Part 2
Primary Processes in Photocatalysis

CHAPTER 7

Kinetic Processes in the Presence of Photogenerated Charge Carriers

YOSHIO NOSAKA*[a] AND ATSUKO Y. NOSAKA[a]

[a]Nagaoka University of Technology, Kamitomioka, Nagaoka, 940-2188 Japan
*E-mail: nosaka@nagaokaut.ac.jp

7.1 Outline of the Processes in Photocatalysis

7.1.1 Environmental Clean-up or Solar Hydrogen Production

Since the discovery of photoinduced water splitting on TiO_2 electrodes in 1972,[1] several studies on photocatalysis by TiO_2 have focused on the solar energy conversion for hydrogen production. Recently, the TiO_2 photocatalysts have been practically devoted to environmental clean-up by decomposing organic pollutants. The difference in these two kinetic processes could be schematically illustrated in Figure 7.1.

Though the electrons photogenerated in the conduction band (CB) are consumed to reduce protons for water splitting, they are actually used to reduce oxygen in air for environmental clean-up. Instead, for water splitting, holes generated in valence band (VB) by four photons are used to oxidize water, while for environmental clean-up only one hole is required to oxidize organic pollutants. Thus, there are varieties of kinetic processes in photocatalysis

RSC Energy and Environment Series No. 14
Photocatalysis: Fundamentals and Perspectives
Edited by Jenny Schneider, Detlef Bahnemann, Jinhua Ye, Gianluca Li Puma, and Dionysios D. Dionysiou

Published by the Royal Society of Chemistry, www.rsc.org

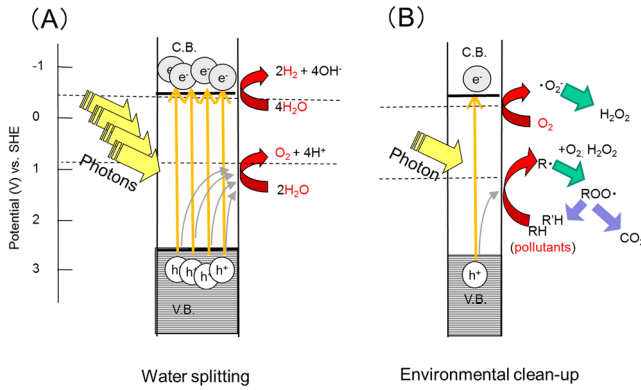

Figure 7.1 Difference in the representative two applications of photocatalytic reactions, (A) water splitting and (B) environmental clean-up.

and the initially employed reactants are also considerably diverse for individual applications. Therefore, in photocatalytic reactions, the primary processes of the photogenerated charge carriers are important. Though there are many review reports concerning the reactions of TiO_2 photocatalysts,[2–7] in the present chapter the primary reaction processes studied mainly in our research group will be reviewed in particular by focusing on the application to environmental clean-up.

7.1.2 Energy Levels of TiO_2 and Water

Figure 7.2(A) shows the pH dependence of standard electrode potential[8] for chemical species involved in four-step reduction from O_2 to H_2O. When the redox reaction involves H^+ or OH^-, the potential shifts depending on the solution pH by −0.059 V per pH unit according to the Nernst's equation. In Figure 7.2(A), the slim dot-dash-line marked with (2e) shows a two-electron process, which is the average of the corresponding two processes of one-electron transfer. The other lines are one-electron redox potentials, which bent at the pK_a of the corresponding species. Namely, $^{\bullet}O_2^-$ is protonated at pH 4.8, while H_2O_2 and $^{\bullet}OH$ are deprotonated at pH 11.7 and 11.9, respectively. Figure 7.2(B) shows relative free energy for chemical species involved in the four-step reduction from O_2 to H_2O at pH 0. Though the redox potentials were measured in homogeneous solution, they could be used as references for considering the primary kinetic processes at the surface of the photocatalyst.

Figure 7.2(A) also shows the edge of the conduction band (CB) and the valence band (VB) of TiO_2 for two crystal phases, *i.e.*, anatase (A-TiO_2) and rutile (R-TiO_2). The potential energies of CB and VB are different between the two phases of TiO_2. According to a recent report,[9] the CB of anatase TiO_2 is lower by 0.22 eV than that of rutile TiO_2, which contradicts results based on the measurements of flat band potential[10] and used in the literatures for decades. However, this novel idea had already been suggested by a report on

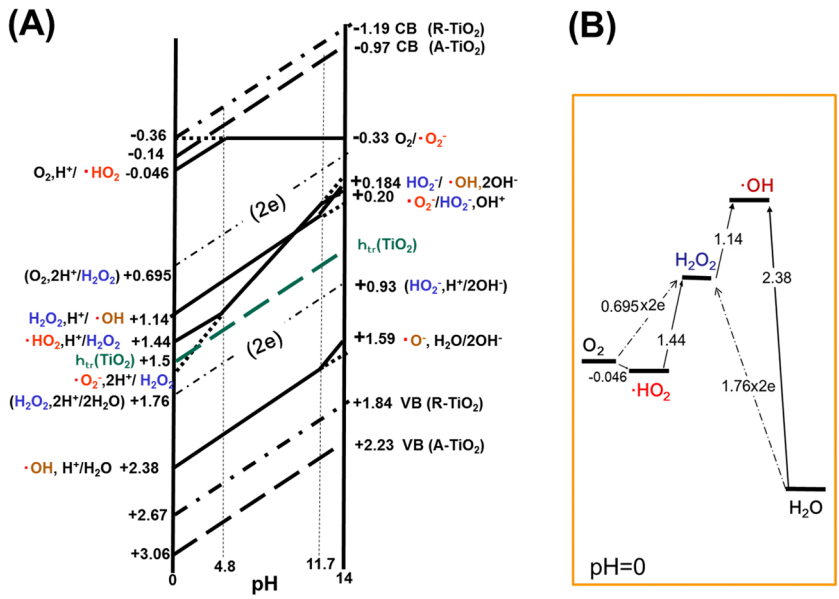

Figure 7.2 (A) pH dependences of conduction band (CB) and valence band (VB) of rutile (R) and anatase (A) TiO_2. The redox potentials (*versus* NHE) of chemical species are also expressed in the reduction steps from O_2 to H_2O. The trapped holes are expressed by h_{tr}. (B) Relative free energy change (in unit of eV) for four-electron reduction of O_2 to H_2O.

the calculated stability of polarons in the two phases of TiO_2, where the holes are favourably located in bulk rutile, while electrons prefer bulk anatase.[11] The potential of the CB edge of rutile TiO_2 shown by heavy dot-dash-lines in Figure 7.2(A) was calculated from recently published data for the flat-band potential of two faces of a rutile single crystal, that is −0.31 V *vs.* Ag/AgCl in 0.1 M $HClO_4$.[12] The energy difference between the CB edge and the flat band potential was estimated to be 0.27 V from the donor density of 8×10^{14} cm^{-3} by employing the reported data[12] and the effective density of the states at the rutile CB edge, which is assumed to be 2.5×10^{19} cm^{-3}.[13]

In Figure 7.2(A), the redox potential of trapped holes was estimated as that of the adsorbed ·OH radicals which were produced by pulse radiolysis technique.[14] Further discussion will be presented later in Section 7.3.3.

7.1.3 Adsorption of Water Molecules

When photocatalytic reactions proceed in water, the reaction kinetics may be different from those performed in air. However, under air the surface of TiO_2 is covered with several layers of water molecules.[15] Therefore, the difference may be related only to the diffusion processes of the molecules involved in the reaction; namely, diffusion in liquid phase or in gas phase.

Upon raising the temperature in ambient environments, the variation in the states of water adsorbed on the TiO_2 powder could be observed as the

change of the proton NMR signals of the water. The TiO_2 surface is covered with three water layers containing distinct water species: (I) the innermost layer with highly immobilized water, (II) the intermediate layer consisting of relatively mobile water, and (III) the outermost layer with mobilized water under the chemical exchange with water vapour.

To elucidate the proper photocatalytic kinetics, the processes of the incorporation of the organic pollutants into these three adsorbed water layers must be taken into account (Figure 7.3a). For instance, by employing ethanol as a pollutant, by solid state NMR measurements it was revealed that the ethanol molecules were initially incorporated into the outermost physisorbed water layer, and stabilized by the hydrogen bonds with water molecules (Figure 7.3b), where both ethanol and water molecules were fairly mobile.[16] By increasing temperature up to 423 K (Figure 7.3c), with the evaporation of water molecules in the outermost layer, the ethanol molecules, which can reach the solid surface and react with titanol to form ethoxide, remain in the inner water layer. Since water and ethanol form an azeotropic mixture, ethanol could remain in the innermost water

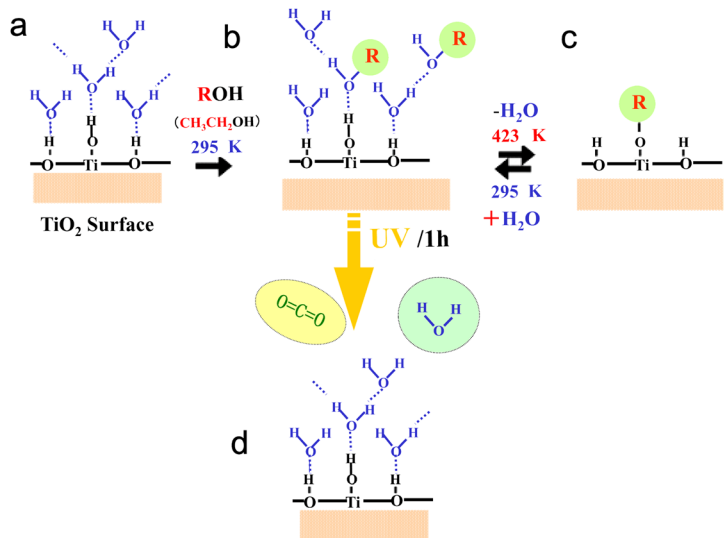

Figure 7.3 Schematic illustration of the incorporation of ethanol into the water layer at the TiO_2 surface and photocatalytic decomposition in air. (a) TiO_2 surface with water. (b) Ethanol molecules loaded preferably stay in the mobile physisorbed water layers. (c) On increasing temperature up to 423 K, water molecules in the inner phase would be replaced successively by ethanol and the ethanol molecules reaching the solid surface react with titanols to form ethoxide. At room temperature, the powder gradually re-adsorbs water molecules in the air and the ethoxide is hydrolyzed to ethanol, which returns to state b. (d) Photo-catalytic reactions of ethanol under atmospheric conditions take place in this state of the reactant, which decomposes to CO_2 and water via several intermediate species.[16] (Reprinted with permission from ref. 16. Copyright 2003 American Chemical Society.)

layer. When the temperature of the powder was decreased to room temperature, it gradually re-adsorbs water molecules from the air to form the water layers, where the formed ethoxide is hydrolysed to ethanol. Consequently, the original state (b) is reversed. Photocatalytic reactions of ethanol under atmospheric conditions proceed in state (b) under UV irradiation and the incorporated reactants (ethanol) would decomposes to CO_2 and water (Figure 7.3d).[16]

7.2 Primary Processes of Photogenerated Charge Carriers

7.2.1 Trapping of Free Charge Carriers

Upon UV irradiation an electron–hole pair, consisting of two free carriers, is produced in a TiO_2 crystallite. The free electron in rutile remains at small polaronic state, resulting in the large effective mass of about $20m_0$.[13] On the other hand, the electron mass in anatase is about m_0. The effective mass of a hole in anatase nanoparticles was estimated to be $0.01m_0$,[17] and that in rutile is suspected to be less than that of the CB electron.[2]

Each carrier in this mobile electron–hole pair is trapped inside or at the surface of the semiconductor solid as a trapped hole and as a trapped electron, respectively. These trapped charge carriers could be identified by the transient absorption spectra as shown in Figure 7.4(A);[18] the assignments of the absorption bands are illustrated in Figure 7.4(B). Besides the transient absorption of trapped electrons, a transient absorption of conducting electrons, which continuously increases with the wavelength in IR region, was observed (blue dotted line in Figure 7.4(A)). The electrons trapped below the CB show a broad absorption band at about 700 nm as illustrated by the yellow arrow in Figure

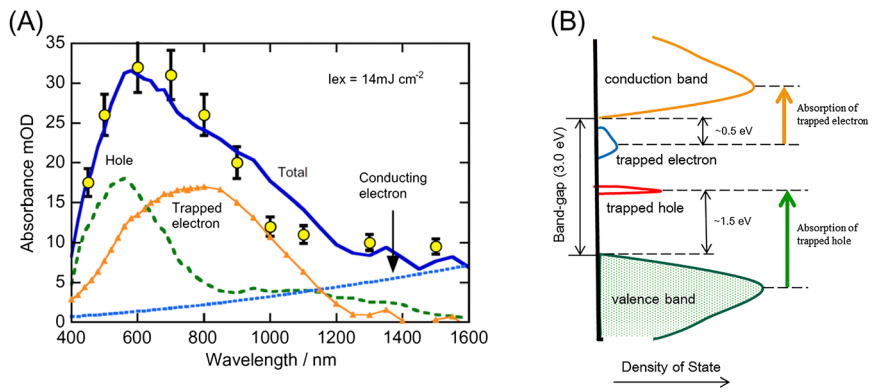

Figure 7.4 (A) Transient absorption spectra for TiO_2 film recorded immediately after excitation with a 355 nm picosecond laser pulse.[18] (Reprinted with permission from ref. 18. Copyright 2010 Elsevier.) (B) Schematic illustration showing energy levels of the trapped carriers and the corresponding absorption band in (A).

7.4(B). On the other hand, the hole-trapping sites are located in the middle of the band gap. As shown in Figure 7.4(B), the absorption band of trapped holes at 500 nm (~2.5 eV) indicates the transitions from the maximum density of the VB state to a trapped state. This absorbance may be also assigned to the transition from a partially occupied trapped state to the maximum density of the CB state, because the band gap is 3.0–3.2 eV. Since the holes behave as electron acceptors, the assignment that the electron in the valence band is excited to the trapped hole state seems appropriate. The potential of the hole trapping site agreed with the reports that the luminescence wavelength of the trapped holes is 810 nm (1.5 eV).[19] The trapped holes were assigned to Ti–O$^{\bullet}$ formed by the dissociation of the Ti–O–Ti bond in the TiO_2 lattice. Moreover, the number of trapped electrons decreased proportionally with the excitation intensity, while the number of the trapped holes only changed slightly[18] indicating that the trapped holes decay independently from the trapped electrons.

The transient absorption properties of 17 commercially available TiO_2 photocatalysts have also been investigated by femtosecond diffuse-reflectance spectroscopy.[20] The transient absorption spectra and the time profile of trapped holes are shown in Figure 7.5 for two representative TiO_2, *i.e.*,

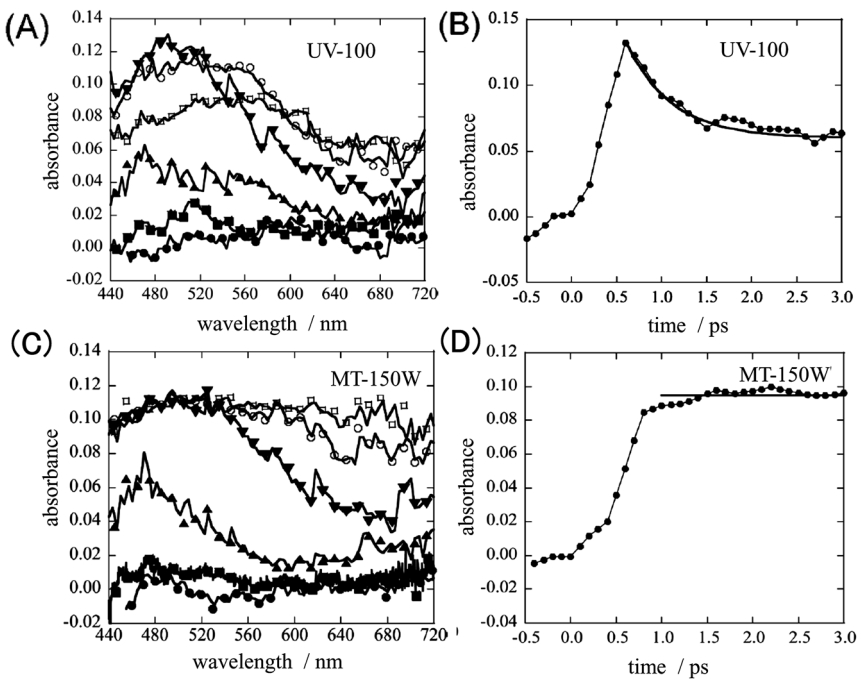

Figure 7.5 (A and C) Typical examples of time-resolved transient absorption spectra for anatase (UV-100) and rutile (MT-150W) TiO_2 powders at various delay times; (●) 0.1, (■) 0.3, (▲) 0.8, (▼) 1.2, (○) 1.4, and (■) 1.8 ps after the 200 fs laser excitation. (B and D) Temporal profiles of the transient absorption at 470 nm for anatase (B) and rutile (D) TiO_2 powders.[20] (Reprinted with permission from ref. 20. Copyright 2011 Taylor & Francis Ltd.)

UV-100 (anatase) and MT-150W (rutile). The trapped holes are formed after the excitation within the experimental time resolution of 0.5 ps, which is consistent with the hole trapping time at the surface of colloidal TiO_2 particles, ~50 fs.[21] The total amount of trapped electrons became smaller with increasing particle size for pure-anatase and pure-rutile TiO_2.[20] For anatase–rutile mixed TiO_2 photocatalysts, the amount of trapped electrons was smaller as compared with those for the pure-anatase and pure-rutile TiO_2 photocatalysts.[20] The initial decay of the trapped holes observed for anatase TiO_2 became slower when it was mixed with rutile TiO_2.[20] This observation agrees with the result of the theoretical calculations, which shows that the holes are thermodynamically more stable in rutile than in anatase TiO_2.[11]

7.2.2 Trapped Electrons and Reduction of O_2

Electrons are trapped as Ti^{3+} in the TiO_2 lattice as shown by ESR measurements.[22] The electron trapping takes place with a time constant of 200 fs.[21] The life time of the trapped electrons can be very long, particularly when holes are consumed, and electrons do not react with scavengers such as O_2. Since the shallowly trapped electrons can be de-trapped to become conducting electrons, the IR absorption of the conducting electrons could be used to monitor the photocatalytic reduction process.

Figure 7.6 shows the decay of the absorbance measured at 2000 cm^{-1} in the presence and the absence of 10 Torr of (A) O_2 and (B) H_2O.[23] The absorbance of conducting electrons in CB decays in the presence of O_2 (Figure 7.6(A)), indicating that the adsorbed O_2 was reduced by free electrons at the time scale of tens μs to form $^{\bullet}O_2^-$. Since the absorbance of free electrons decays very slowly, trapping and de-trapping of electrons may take place in the absence of O_2. In vacuum, the decay is extremely slow as shown in Figure 7.6(B) on a larger time scale, which could be ascribed to the consumption of electrons resulting from the recombination with holes. Notably, the decay declined in the presence of H_2O vapour. This deceleration of the decay in the presence of water is ascribed to the consumption of the holes by the oxidation of water.

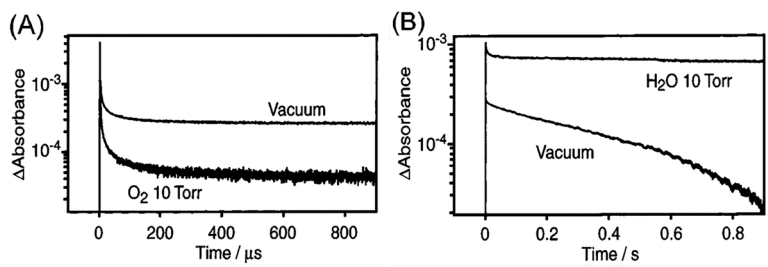

Figure 7.6 Transient IR absorption measured at 2000 cm^{-1} for conducting electrons in TiO_2 induced by the 355 nm pump pulse, in the presence and the absence of 10 Torr of (A) O_2 and (B) H_2O.[23] (Reprinted with permission from ref. 23. Copyright 2001 American Chemical Society.)

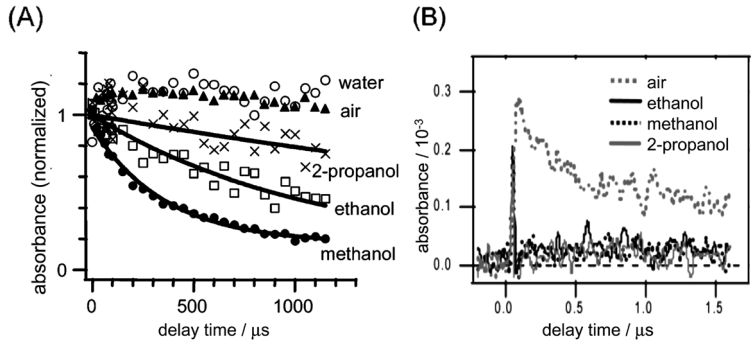

Figure 7.7 Transient absorption of trapped holes (A) measured at 400 nm with a 160 fs laser and (B) measured at 415 nm with an 8 ns laser excitation at 355 nm for anatase-TiO_2 nanocrystalline film in air, methanol, ethanol, and 2-propanol.[24] (Reprinted with permission from ref. 24. Copyright 2006 American Chemical Society.)

7.2.3 Trapped Holes and Oxidation of Alcohols

Figure 7.7 shows the decay of the trapped holes in the presence of alcohols.[24] In Figure 7.7(A), the absorbance just after excitation did not change after the addition of water, indicating that the photogenerated holes did not react with water but with different alcohols. As shown in the Figure 7.7(B), the oxidation of adsorbed alcohols occurred within 8 ns of the pulse duration. Figure 7.7(A) shows various decay rates in the time scale of ps, indicating the difference in the reaction rate for each alcohol. In air, trapped holes decay slowly by the recombination with electrons, which is consistent with the decay of electrons.[22]

7.3 Kinetic Processes at Pure TiO_2 Photocatalysts

7.3.1 O_2 Production at Rutile Surfaces

It has long been supposed that the water photo-oxidation and photocatalytic oxidation of organic compounds were accompanied by $^{\bullet}OH$ radical production.[3] In photocatalysis, it is difficult to investigate the oxidation process separately, because it is affected simultaneously both by the reduction process and by the electron–hole recombination. On the other hand, a photoelectrochemical process has advantages in terms of investigating oxidation only and allowing the measurement of reaction rates as electric current.

Figure 7.8(A) shows the current–time curves obtained under UV light irradiation for three distinct single crystalline rutile TiO_2 electrodes *i.e.*, (100), (110), and (001).[25] Only for the (100) electrode did the photocurrent decrease initially and then became constant. Since the initial photocurrent could recover after holding the electrode in the dark at the rest potential, tentatively, the anodic polarization changed the surface properties of the (100) face thus decreasing the photocurrent. Presumably, OH^- anions were adsorbed on the surface by applying potential, then the surface reversed to the initial state by desorption. The electric charge of the photocurrent was measured by integrating the

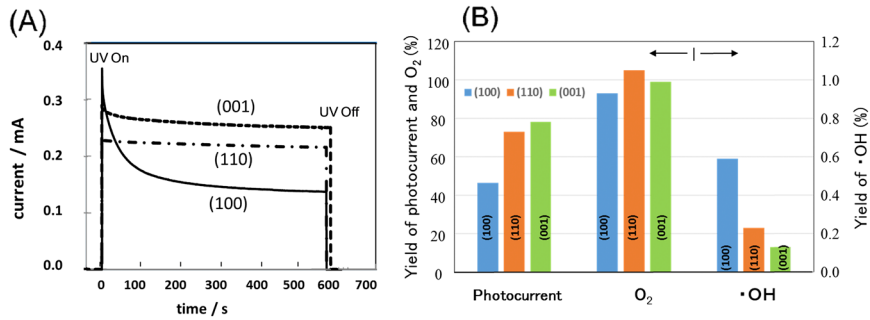

Figure 7.8 (A) Time profiles of the photocurrent during O_2 measurements at 1.3 V (*versus* Ag/AgCl) for rutile TiO_2 electrodes of distinct crystalline faces: (100), (110), and (001).[25] (B) Yields of the photocurrent averaged for 30 min of O_2 and of $^{\bullet}OH$.[25] (Reprinted with permission from ref. 25. Copyright 2013 American Chemical Society.)

photocurrent, and the yield of photocurrent was estimated from the electric charge by dividing by the amount of absorbed photons (Figure 7.8(B)). The amount of evolved O_2 was measured and the yield (current efficiency) of O_2 formation was calculated with the electric charge. The O_2 yield was found to be about 100% (Figure 7.8(B)). The concentration of $^{\bullet}OH$ radicals produced under the same conditions was measured by a coumarin fluorescence probe method, and the $^{\bullet}OH$ radical yield was calculated (Figure 7.8(B)).

The higher yield of photocurrent for (001) TiO_2 indicates a faster O_2 production, while the yield of $^{\bullet}OH$ radicals for this crystal was the smallest. On the other hand, for the (100) surface, O_2 production was the slowest among the three electrodes, while the $^{\bullet}OH$ radical yield was the largest. This observation suggests that, when O_2 formation is not feasible for some reason, $^{\bullet}OH$ radicals should be produced at the rutile TiO_2 surface. In other words, $^{\bullet}OH$ radicals were formed as a by-product in the process of O_2 production. In the oxidation process of water at the rutile surface, the two-electron oxidation intermediate was assigned to Ti–O–O–Ti peroxo complexes.[26] Therefore, we could illustrate the difference in the reaction processes of O_2 production and $^{\bullet}OH$ radical formation as shown in Figure 7.9. The difference could be explained by the difference in the strength of the Ti–O bond of the peroxo intermediate against hole attack. Namely, O_2 would be formed when the Ti–O bond in Ti–O–O–Ti breaks as shown in path (a). On the other hand, $^{\bullet}OH$ radicals are formed when the O–O bond is cleaved (b) instead of the Ti–O bond. Since, for the ideal surface of (100), the Ti–O–O–Ti group exists in a symmetric structure, the Ti–O bond is more rarely broken as compared to the other facets, leading to a higher yield of $^{\bullet}OH$ radicals.[25]

7.3.2 $^{\bullet}OH$ Radical Formation over Rutile and Anatase Photocatalysts

The difference in $^{\bullet}OH$ radical generation through photocatalytic reaction with distinct crystalline types of TiO_2 in aqueous suspension was explored by means of a fluorescence probe method. Figure 7.10(A) shows the formation

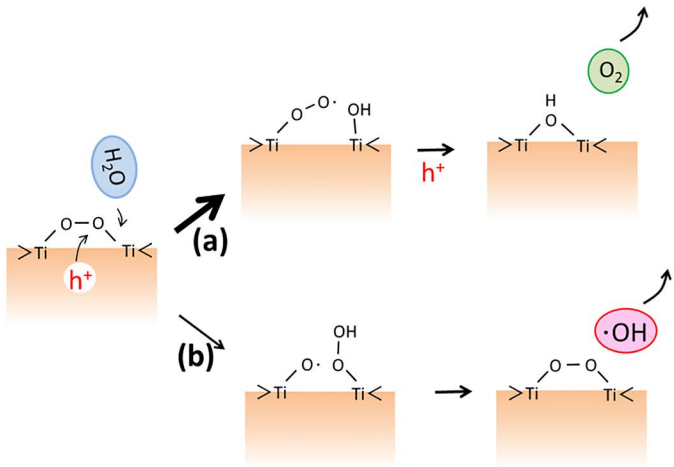

Figure 7.9 Plausible reaction steps starting from Ti-peroxo complex to form (a) O_2 and (b) ·OH at the rutile TiO_2 surface.[25] (Reprinted with permission from ref. 25. Copyright 2013 American Chemical Society.)

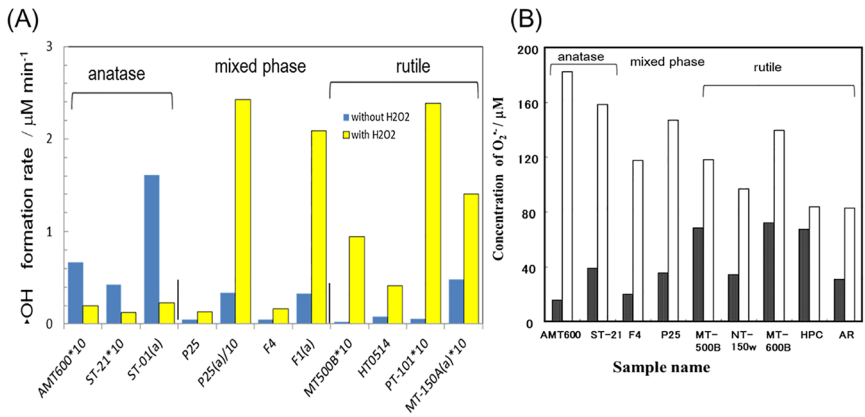

Figure 7.10 (A) Effect of H_2O_2 on ·OH radical formation. In the presence (yellow bar) and in the absence (blue bar) of H_2O_2.[27,28] The scale was adjusted by multiplying by 10 (×10) or dividing by 10 (/10) as suitable for each sample. (B) Effect of H_2O_2 on $\cdot O_2^-$ formation. In the presence (white bar) and the absence (dark bar) of 0.2 mM H_2O_2.[27] (Reprinted with permission from ref. 27. Copyright 2007 Elsevier.)

rate of ·OH radicals measured by a terephthalic acid probe method in the presence (yellow bar) and in the absence (blue bar) of 0.2 mM H_2O_2.[27,28] For the samples marked with (a), the measurements were performed by a coumarin-3-carboxylic acid probe method with and without 0.14 mM of H_2O_2.[28] Rutile TiO_2 produced a much smaller amount of ·OH radicals as compared to

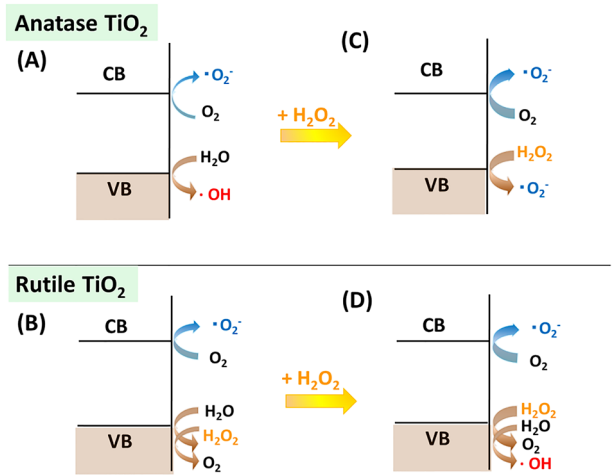

Figure 7.11 Photocatalytic processes at TiO_2 with anatase and rutile crystalline types in the absence of H_2O_2 (A) and (B) and in the presence of H_2O_2 (C) and (D), respectively. The thickness of arrows expresses the degree of the reaction rate.[28] (Reprinted with permission from ref. 28. Copyright 2014 American Chemical Society.)

anatase and mixed-phase TiO_2. In the presence of H_2O_2 the $^{\bullet}OH$ radical generation for the pure anatase TiO_2 decreased but increased for rutile and mixed-phase TiO_2. The formation of $^{\bullet}OH$ radicals from H_2O_2 is usually explained by the reduction by CB electrons. However, the formation of $^{\bullet}O_2^-$ was not decreased in the presence of H_2O_2 (Figure 7.10(B)). Then the addition of H_2O_2 accelerated the oxidation of water to $^{\bullet}OH$ radicals.

Therefore, the difference between the photocatalytic reaction of water and that of oxygen is illustrated in Figure 7.11. On the surface of anatase, photoinduced VB holes generate $^{\bullet}OH$ radicals, while at the surface of rutile TiO_2 water is initially oxidized to H_2O_2 and then further oxidized to O_2.[25] In the generation process of O_2, a certain amount of $^{\bullet}OH$ radicals could be produced as depicted in Figure 7.8. On the other hand, electrons in the CB can reduce O_2 to $^{\bullet}O_2^-$ and the latter may become H_2O_2 by disproportionation.[27] As illustrated on the right-hand side in Figure 7.11, when H_2O_2 is added into these reaction systems, for anatase TiO_2, the oxidation of H_2O is replaced by the oxidation of H_2O_2 to produce $^{\bullet}O_2^-$ because the redox potential of H_2O_2 is less positive than that of H_2O as shown in Figure 7.2(A). Then, $^{\bullet}OH$ generation is suppressed and $^{\bullet}O_2^-$ formation is accelerated with H_2O_2 (Figure 7.10(B)). For rutile TiO_2, since the surface is preferable for the O_2 generation, H_2O_2 is readily oxidized to O_2 and then $^{\bullet}OH$ radicals are produced as a by-product. This oxidation of H_2O_2 would accelerate the reduction of O_2 to form $^{\bullet}O_2^-$.[29]

Based on the above observations, the detailed generation mechanisms of $^{\bullet}OH$ radicals on anatase and rutile TiO_2 surfaces can be proposed as shown in

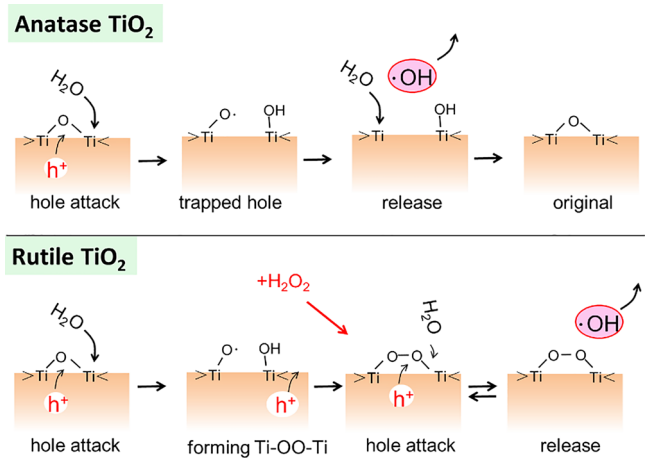

Figure 7.12 Plausible mechanisms of ·OH generation at anatase TiO_2 (upper), and rutile TiO_2 (lower). Note that the surface Ti-peroxo complex can be formed by the adsorption of H_2O_2 for rutile TiO_2.[28] (Reprinted with permission from ref. 28. Copyright 2014 American Chemical Society.)

Figure 7.12. On the anatase surface, the photogenerated valence band holes, h^+, are trapped at the surface oxygen to form trapped holes (Ti–O·) which can be regarded as adsorbed ·OH in the deprotonated form (·O^-);[30] subsequently an ·OH radical is released. Though the release of the ·OH radicals has been shown to be thermodynamically hindered[31] their release at the surface of TiO_2 has been demonstrated by a laser-induced-fluorescence method.[32] In contrast, for rutile TiO_2, since the crystalline structure is packed more tightly than that for anatase TiO_2, the stability of the surface trapped holes may be different. According to the reaction mechanism of water oxidation for rutile TiO_2,[33] Ti-peroxo species are formed by trapping h^+ near the trapped hole. Since Ti-peroxo species are equivalent to the adsorbed H_2O_2,[26] the increase of ·OH generation with H_2O_2 for rutile TiO_2 can be explained.

7.3.3 Kinetics of Methanol Oxidation

To elucidate the photocatalytic oxidation process, free ·OH radicals in photocatalysis were monitored by a fluorescence probe method in the presence of reactants (A), such as alcohols (MeOH and EtOH) and inorganic ions (I^-, Br^- and SCN^-).[34] The reaction processes can be modelled with eqn (7.1)–(7.6), where coumarin (Cou) reacts with free ·OH radicals to form fluorescent OH–Cou (7.5) to be detected. The question is whether the reactant A is oxidized directly by trapped holes (7.2) or by free ·OH radicals (7.6) which are produced in the solution *via* the trapped holes (7.3). The reaction rate of A with free ·OH radicals could be measured from the formation rate of OH–coumarin (OH–Cou) by changing the concentration of the reactant A. To fit the experimental results, the reverse reaction of free ·OH formation, namely the reaction

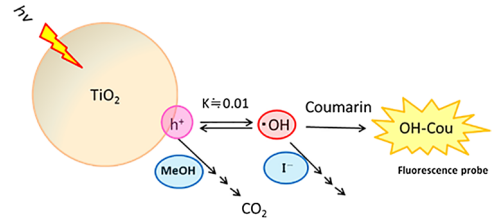

Figure 7.13 Plausible photocatalytic oxidation processes for methanol and iodide ions deduced from •OH radical detection with coumarin fluorescence probe.[34] (Reprinted with permission from ref. 34. Copyright 2014 Elsevier.)

in which the trapped holes are generated with the adsorption of free •OH radicals (7.4), should be involved:

$$TiO_2 + h\nu \xrightarrow{g'} h^+ \longrightarrow TiO_2 + h\nu \tag{7.1}$$

$$h^+ + A \xrightarrow{k_A'} \text{product} \tag{7.2}$$

$$h^+ + OH^- \xrightarrow{k_0} {}^{\bullet}OH \tag{7.3}$$

$${}^{\bullet}OH \xrightarrow{k_h} h^+ + OH^- \tag{7.4}$$

$${}^{\bullet}OH + \text{Cou} \xrightarrow{k_c} \alpha\cdot\text{OH–Cou} \tag{7.5}$$

$${}^{\bullet}OH + A \xrightarrow{k_A} \text{product} \tag{7.6}$$

On the basis of the set of the reactions (7.1)–(7.6), by using a steady-state approximation to h^+ and free •OH, the concentration of OH–Cou produced after the irradiation time of t can be expressed by eqn (7.7):[34]

$$\frac{1}{[\text{OH–Cou}]_t} = \frac{k_0}{t\cdot g'\cdot\alpha} + \frac{k_A'\left(k_h + k_c[\text{Cou}]\right)}{t\cdot g'\cdot\alpha\cdot k_c[\text{Cou}]}\cdot[A] \tag{7.7}$$

By analysis of the reaction with inorganic ions, the photocatalytic oxidation was found to proceed through free •OH radicals for inorganic ions. On the other hand, for the organic molecules it has been suggested that the oxidation should not be caused by the free •OH radicals but by the holes trapped on the TiO_2 surface.[34] This conclusion is supported by the fact that the quantum efficiency of CO_2 formation by MeOH oxidation was ten times larger than that of the free •OH formation.[34] A general scheme of the photocatalytic oxidation and probing of •OH radicals with coumarin is illustrated in Figure 7.13. Based on the kinetic analysis of the dependence on the coumarin concentration, the photogenerated •OH radicals in solution are most probably in equilibrium with the holes trapped on the TiO_2 surface. By assuming a diffusion control for the reaction of MeOH with h^+, the equilibrium constant ($=k_0/k_h$) could be estimated to be about 0.01.[34]

The above discussion along with a previous study[30] would lead to the implication that the generated free $^{\bullet}OH$ radicals could be trapped on the TiO_2 surface. Trapping of $^{\bullet}OH$ radicals was suggested in 1991 with the use of pulse radiolysis experiments, where the reaction of $^{\bullet}OH$ produced by electron-beam irradiation in TiO_2 suspension was found to form surface trapped holes:[14]

$$^{\bullet}OH \leftrightarrow {}^{\bullet}O^{-} + H^{+} \ (pK_a = 11.9) \quad (7.8)$$

$$^{\bullet}OH + \equiv Ti^{4+} \leftrightarrow \equiv Ti^{4+}O^{\bullet -} + H^{+} \ (\Delta G \approx -39 \text{ kJ mol}^{-1}) \quad (7.9)$$

Although the proton dissociation constant of $^{\bullet}OH$ in eqn (7.8) in homogeneous solution is reported to be $pK_a = 11.9$,[8] the pK_a of $^{\bullet}OH$ shifts to $pK_a = 2.8$ in the state adsorbed on TiO_2, because the charge density shifts to the lattice oxygen.[14] In other words, at neutral pH, $^{\bullet}OH$ is adsorbed dissociatively in the form of a trapped hole as shown by eqn (7.9). The trapped holes could not react with coumarin to produce OH–coumarin but react with organic reactants, such as methanol. The redox potential of the trapped holes was experimentally obtained to be *ca.* 1.5 V (V *versus* NHE).[14] Since the redox potential of $^{\bullet}OH$ is 1.90 V,[35] the adsorption of $^{\bullet}OH$ on TiO_2 in aqueous solution, eqn (7.9), is exo-energetic by about 0.4 eV or 39 kJ mol^{-1}. Thus, the $^{\bullet}OH$ in solution becomes the surface trapped hole by adsorption, because protons are released owing to the shift of the pK_a associated with the adsorption.

7.4 Modified TiO_2 Photocatalysts for Visible Light Response

7.4.1 Copper(II) deposited TiO_2 and WO_3

To utilize TiO_2 photocatalysts in indoor environments, visible-light responsive photocatalysts prepared by the modification of TiO_2 have been studied. The reaction processes of Cu(II)/TiO_2 and Cu(II)/WO_3 photocatalysts are proposed and illustrated in Figure 7.14.[29] By grafting metal ions on the TiO_2 surface, the visible-light absorption was achieved by the interfacial charge transfer (IFCT) from the TiO_2 VB to the grafted metal ions.[36,37] The reaction processes of visible-light responsive Cu(II)-grafted TiO_2 and WO_3 photocatalysts were analysed by detecting the trapped holes and electrons by means of ESR spectroscopy, and $^{\bullet}O_2^{-}$ and H_2O_2 by chemiluminescence photometry. The reduction of grafted Cu^{2+} and the alternative reduction of O_2 by the thus formed Cu^{+} were elucidated by ESR measurements at 77 K for both photocatalysts under the irradiation of visible light. The one-electron reduction product of O_2, *i.e.*, $^{\bullet}O_2^{-}$, was detected in aqueous suspension of Cu(II)/TiO_2. Contrary to the case of UV-irradiated bare TiO_2, the formation of $^{\bullet}O_2^{-}$ was suppressed by the addition of H_2O_2. The decrease in $^{\bullet}O_2^{-}$ formation with the addition of H_2O_2 suggests that H_2O_2 should be reduced to $^{\bullet}OH$ radicals at the Cu^{2+}/Cu^{+} level, because the reduction of H_2O_2 occurs more preferably than that of O_2 as indicated in Figure 7.2. For Cu(II)/WO_3, since the optical

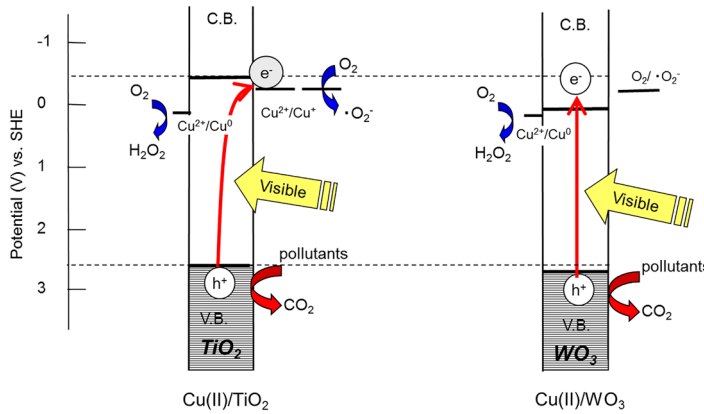

Figure 7.14 Energy diagram of Cu(II)-grafted TiO_2 (rutile) and WO_3 photocatalysts at pH 7, showing the photocatalytic reaction processes under visible light irradiation.[29] (Reprinted with permission from ref. 29. Copyright 2014 American Chemical Society.)

absorption is mainly caused by band-gap excitation, only the two-electron reduction product, H_2O_2, was observed,[29] with Cu^{2+} species acting as catalysts.

7.4.2 Iron(III)-deposited Ru-doped TiO_2

Since the absorption coefficient of IFCT of Cu(II) and Fe(III) deposited TiO_2 is very small, the combination of metal ion doping *via* deposition has been developed to promote the visible light absorption.[38] The photocatalytic reaction processes of Fe(III)-grafted TiO_2 (Fe/TiO_2) and Fe(III)-grafted Ru-doped TiO_2 (Fe/Ru:TiO_2) were clearly elucidated by means of ESR spectroscopy and by chemiluminescence photometry.[39]

By ESR spectroscopy it was revealed that visible-light irradiation on the Fe/TiO_2 photocatalyst caused the direct charge transfer from the valence band of TiO_2 to the grafted Fe ions. For the Fe/Ru:TiO_2 photocatalyst, acceptor levels were formed by doping Ru ions in the lattice of TiO_2, because Ru^{3+} could be observed in the ESR spectra upon visible-light irradiation. In the presence of Fe(III), the electrons at the acceptor level are readily transfered to Fe(III) ions with recovery of Ru^{4+}, then the signal of Ru^{3+} was not observed for Fe/Ru:TiO_2.[39] In this case, the decrease in the ESR signal of Fe^{3+} was accordingly detected.[39]

Moreover, by chemiluminescence photometry it was confirmed that the grafted Fe ions act as a promoter to reduce O_2 to H_2O_2 *via* two-electron reduction. Since longer-wavelengths of light ($\lambda > 500$ nm) induced the formation of the conduction band electrons, a two-step electron excitation from the valence band to the conduction band through defect levels such as oxygen vacancy (V_O) was proposed as shown in Figure 7.15. However, it was implied that V_O levels were not effective for visible-light photocatalytic activity.[40]

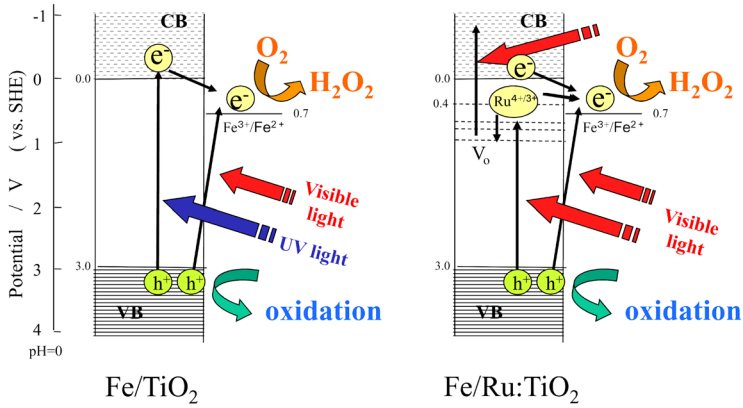

Figure 7.15 Suggested reaction mechanisms of visible-light-responsive photocatalysis for Fe(III)-deposited TiO_2 and Fe(III)-deposited Ru(IV)-doped TiO_2. V_O: oxygen vacancy.[39] (Reprinted with permission from ref. 39. Copyright 2012 American Chemical Society.)

7.4.3 Platinum Complex Sensitized TiO_2

To provide visible-light response of TiO_2 photocatalysts, dye sensitization type photocatalysts such as platinum(IV)-hexachloride deposited TiO_2 (PtCl/TiO_2) have been proposed.[41,42] The reaction process of PtCl/TiO_2 photocatalysts under visible-light irradiation was examined by means of ESR spectroscopy and chemiluminescence photometry.[43]

The photoinduced trapped electrons and holes were detected at 77 K by ESR spectroscopy. The ESR signal of Pt^{3+} was also observed under visible-light ($\lambda > 500$ nm) irradiation, indicating that a charge separation was induced in the deposited PtCl yielding Pt^{3+} and Cl radicals. Upon light irradiation, ESR signals appeared, which can be attributed to the holes trapped at the subsurface lattice oxygen. Notably, even under visible-light ($\lambda > 500$ nm) irradiation, the PtCl/TiO_2 produced a significant amount of trapped holes. This indicates that holes are photogenerated by a process other than inter-band excitation.

Figure 7.16(A) shows the amount of photogenerated $^{\bullet}O_2^-$ and H_2O_2 as a function of the irradiation time for PtCl/TiO_2 in aqueous suspension. The amount of $^{\bullet}O_2^-$ abruptly increased in the initial stage, which could be caused by the reduction of O_2 adsorbed on the surface. The decrease of $^{\bullet}O_2^-$ by further irradiation indicated that the generated $^{\bullet}O_2^-$ could be oxidized to O_2 by photogenerated Cl radicals or by the valence band holes. Thus, as shown in Figure 7.16(B), valence band holes were formed by the electron transfer to the oxidized PtCl upon the visible-light absorption, leading to the high photocatalytic activity of PtCl/TiO_2. Thus, in dye-sensitized TiO_2 photocatalysis, visible-light IFCT excitation to the oxidized dye to produce valence band holes was suggested to be involved in the reaction mechanism.[43]

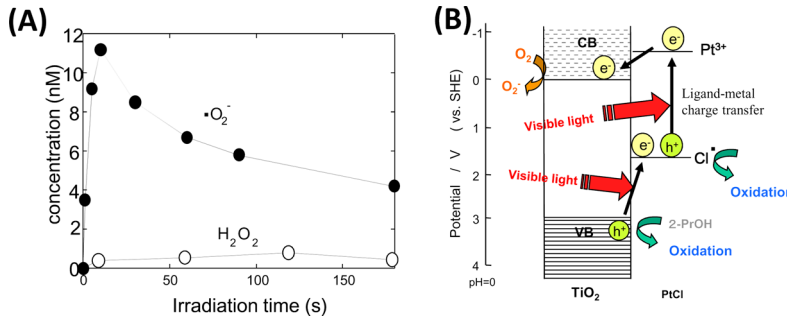

Figure 7.16 (A) Concentrations of (●) $^{\bullet}O_2^-$ and (○) H_2O_2 formed upon irradiation of photocatalysts with 442 nm light. (B) Suggested processes in visible-light-induced reactions for the Pt-complex modified TiO_2 (PtCl/TiO_2) photocatalyst.[43] (Reprinted with permission from ref. 43. Copyright 2012 American Chemical Society.)

7.4.4 Gold-Nanoparticle Deposited TiO_2

Quite recently, gold-nanoparticle-deposited TiO_2 (AuNP/TiO_2) has been anticipated as one of the promising visible-light responsive photocatalysts, where the plasmonic absorption of AuNP plays the role of a photosensitizer.[44] To investigate the primary reaction process causing the photocatalytic activity, we prepared various AuNP/TiO_2 samples using 13 commercially available TiO_2 powders and detected the formation of $^{\bullet}O_2^-$.[45] In Figure 7.17(A) the initial generation rates of $^{\bullet}O_2^-$ are plotted as a function of the primary particle size of TiO_2. In addition to $^{\bullet}O_2^-$, the formation of singlet oxygen ($^1O_2$) was also detected.[46] Hence the reaction process could be illustrated as shown in Figure 7.17(B).

The rate of $^{\bullet}O_2^-$ generation became larger with increasing TiO_2 particle size of AuNP/TiO_2. The samples prepared with anatase TiO_2 showed larger rates than those prepared with rutile TiO_2. These observations could be explained by the following mechanisms, where the plasmonic excited AuNP electrons are transfered to TiO_2 to produce $^{\bullet}O_2^-$ (Step 1). Since the CB potential of anatase is less negative than that of rutile as described above (Section 7.1.2), anatase showed a higher rate of $^{\bullet}O_2^-$ formation with feasible electron transfer from AuNP to TiO_2. For TiO_2 particles of large size, the transferred electrons could diffuse in TiO_2 for a longer period of time to reduce O_2 (Step 2), then the recombination with h^+ in the AuNP would be delayed. The simultanous formation of $^1O_2$ has been explained by the oxidation of $^{\bullet}O_2^-$ (Step 3), based on our previous investigation on the $^1O_2$ formation in the photocatalysis of bare-TiO_2 under UV-irradiation.[47,48]

In Figure 7.18(A), the generated amount of $^1O_2$ is plotted against the corresponding generation rate of $^{\bullet}O_2^-$. The remarkable correlation observed between $^1O_2$ and $^{\bullet}O_2^-$ confirmed the formation of $^1O_2$ from $^{\bullet}O_2^-$ as stated above. In Figure 7.18(A), the mixed phase TiO_2 (marked with the orange triangles) deviated from the dependence of pure crystalline phases of TiO_2 exhibiting a higher $^1O_2$ production rate. The distinctive observation for the

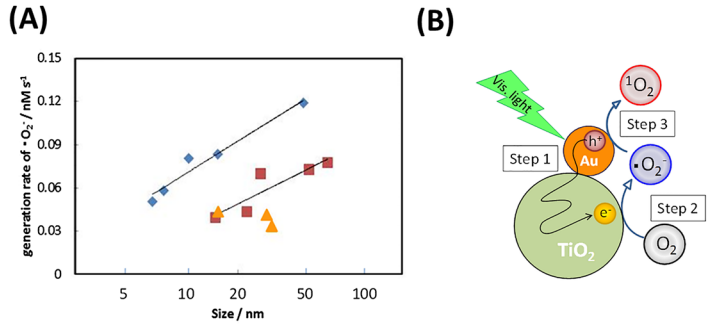

Figure 7.17 (A) Relationship between $^{\bullet}O_2^-$ generation rate and the primary particle size of TiO_2 powders of AuNP/TiO_2. Each crystalline phase of TiO_2 was anatase (♦), rutile (■), and mixed phase (▲). (B) Plausible mechanism for the generation of $^{\bullet}O_2^-$ and $^1O_2$ on AuNP/TiO_2 excited with visible light.[45] (Reprinted with permission from ref. 45. Copyright 2014 American Chemical Society.)

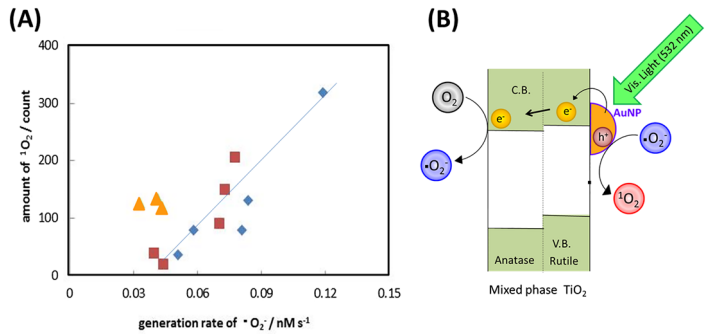

Figure 7.18 (A) Relationship between the amount of $^1O_2$ and the generation rate of $^{\bullet}O_2^-$ for AuNP/TiO_2 with anatase (♦), rutile (■), and mixed phase (▲) crystallites.[45] (Reprinted with permission from ref. 45. Copyright 2014 American Chemical Society.) (B) Stabilization of CB electrons by interphase transfer, leading to the increase of $^1O_2$ formation shown in (A).

mixed phase TiO_2 could be explained by electron transfer from rutile to anatase phase in the particle (Figure 7.18(B)), which prolongs the lifetime of holes in AuNP by preventing the recombination with electrons, resulting in the increase of the oxidation of $^{\bullet}O_2^-$.

It is generally acknowledged that $^1O_2$ could be applied to photodynamic therapy. Since AuNP/TiO_2 is a non-hazardous material, if sufficient generation of $^1O_2$ is attained, AuNP/TiO_2 could be applied to medical use.

References

1. A. Fujishima and K. Honda, *Nature*, 1972, **238**, 37.
2. A. Fujishima, X. Zhang and D. Tryk, *Surf. Sci. Rep.*, 2008, **63**, 515.
3. P. Salvador, *Prog. Surf. Sci.*, 2011, **86**, 41.

4. M. A. Henderson, *Surf. Sci. Rep.*, 2011, **66**, 185.
5. L. Zhang, H. H. Mohamed, R. Dillert and D. Bahnemann, *J. Photochem. Photobiol., C*, 2012, **13**, 263.
6. K. Bourikas, C. Kordulis and A. Lycourghiotis, *Chem. Rev.*, 2014, **114**, 9754.
7. J. Schneider, M. Matsuoka, M. Takeuchi, J. Zhang, Y. Horiuchi, M. Anpo and D. W. Bahnemann, *Chem. Rev.*, 2014, **114**, 9919.
8. *Standard Potentials in Aqueous Solution*, ed. A. J. Bard, R. Parsons and J. Jordan, Marcel Dekker, New York, 1985.
9. D. O. Scanlon, C. W. Dunnill, J. Buckeridge, S. A. Shevlin, A. J. Logsdail, S. M. Woodley, C. R. A. Catlow, J. M. Powell, R. G. Palgrave, I. P. Parkin, G. W. Watson, T. W. Keal, P. Sherwood, A. Walsh and A. A. Sokol, *Nat. Mater.*, 2013, **12**, 798.
10. L. Kavan, M. Graetzel, S. E. Gilbert, C. Klemenz and H. J. Scheel, *J. Am. Chem. Soc.*, 1996, **118**, 6716.
11. N. A. Deskins and M. Dupuis, *J. Phys. Chem. C*, 2009, **113**, 346.
12. E. Tsuji, K. Fukui and A. Imanishi, *J. Phys. Chem. C*, 2014, **118**, 5406.
13. H. Tang, K. Prasad, R. Sanjines, P. E. Schmid and F. Levy, *J. Appl. Phys.*, 1994, **75**, 2042.
14. D. Lawless, N. Serpone and D. Meisel, *J. Phys. Chem.*, 1991, **95**, 5166.
15. A. Y. Nosaka and Y. Nosaka, *Bull. Chem. Soc. Jpn.*, 2005, **78**, 1595.
16. A. Y. Nosaka, T. Fujiwara, H. Yagi, H. Akutsu and Y. Nosaka, *Langmuir*, 2003, **19**, 1935.
17. T. Toyoda and I. Tsuboya, *Rev. Sci. Instrum.*, 2003, **74**, 782.
18. R. Katoh, M. Murai and A. Furube, *Chem. Phys. Lett.*, 2010, **500**, 309.
19. R. Nakamura, T. Okamura, N. Ohashi, A. Imanishi and Y. Nakato, *J. Am. Chem. Soc.*, 2005, **127**, 12975.
20. Y. Murakami, J. Nishino, T. Mesaki and Y. Nosaka, *Spectrosc. Lett.*, 2011, **44**, 88.
21. X. Yang and N. Tamai, *Phys. Chem. Chem. Phys.*, 2001, **3**, 3393.
22. Y. Nakaoka and Y. Nosaka, *J. Photochem. Photobiol., A*, 1997, **110**, 299.
23. A. Yamakata, T. Ishibashi and H. Onishi, *J. Phys. Chem. B*, 2001, **105**, 7258.
24. Y. Tamaki, A. Furube, M. Murai, K. Hara, R. Katoh and M. Tachiya, *J. Am. Chem. Soc.*, 2006, **128**, 416.
25. Y. Nakabayashi and Y. Nosaka, *J. Phys. Chem. C*, 2013, **117**, 23832.
26. R. Nakamura and Y. Nakato, *J. Am. Chem. Soc.*, 2004, **126**, 1290.
27. T. Hirakawa, K. Yawata and Y. Nosaka, *Appl. Catal., A*, 2007, **325**, 105.
28. J. Zhang and Y. Nosaka, *J. Phys. Chem. C*, 2014, **118**, 10824.
29. Y. Nosaka, S. Takahashi, H. Sakamoto and A. Y. Nosaka, *J. Phys. Chem. C*, 2011, **115**, 21283.
30. J. Zhang and Y. Nosaka, *J. Phys. Chem. C*, 2013, **117**, 1383.
31. T. Bredow and K. Jug, *J. Phys. Chem.*, 1995, **99**, 285.
32. Y. Murakami, K. Endo, I. Ohta, A. Y. Nosaka and Y. Nosaka, *J. Phys. Chem. C*, 2007, **111**, 11339.
33. A. Imanishi, T. Okamura, N. Ohashi, R. Nakamura and Y. Nakato, *J. Am. Chem. Soc.*, 2007, **129**, 11569.

34. J. Zhang and Y. Nosaka, *Appl. Catal., B*, 2015, **166–167**, 32.
35. P. Wardam, *J. Phys. Chem. Ref. Data*, 1988, **18**, 1637.
36. H. Irie, K. Kamiya, T. Shibanuma, S. Miura, D. A. Tryk, T. Yokoyama and K. Hashimoto, *J. Phys. Chem. C*, 2009, **113**, 10761.
37. H. Yu, H. Irie, Y. Shimodaira, Y. Hosogi, Y. Kuroda, M. Miyauchi and K. Hashimoto, *J. Phys. Chem. C*, 2010, **114**, 16481.
38. M. Liu, X. Qiu, M. Miyauchi and K. Hashimoto, *J. Am. Chem. Soc.*, 2013, **135**, 10064.
39. M. Nishikawa, Y. Mitani and Y. Nosaka, *J. Phys. Chem. C*, 2012, **116**, 14900.
40. M. Nishikawa, R. Takanami, F. Nakagoshi, H. Suizu, H. Nagai and Y. Nosaka, *Appl. Catal., B*, 2014, **160–161**, 722.
41. G. Burgeth and H. Kisch, *Coord. Chem. Rev.*, 2002, **230**, 41.
42. Y. Ishibai, J. Sato, S. Akita, T. Nishikawa and S. Miyagishi, *J. Photochem. Photobiol., A*, 2007, **188**, 106.
43. M. Nishikawa, H. Sakamoto and Y. Nosaka, *J. Phys. Chem. A*, 2012, **116**, 9674.
44. E. Kowalska, R. Abe and B. Ohtani, *Chem. Commun.*, 2009, 241.
45. H. Saito and Y. Nosaka, *J. Phys. Chem. C*, 2014, **118**, 15656.
46. H. Saito and Y. Nosaka, *Chem. Lett.*, 2012, **41**, 1591.
47. Y. Nosaka, T. Daimon, A. Y. Nosaka and Y. Murakami, *Phys. Chem. Chem. Phys.*, 2004, **6**, 2917.
48. T. Daimon and Y. Nosaka, *J. Phys. Chem. C*, 2007, **111**, 4420.